Electronic Supplementary Information (ESI) for

Near-infrared light-inducible Z-scheme overall water-splitting photocatalyst without an electron mediator

Hiroshi Irie,*[ab] Masaomi Yoda,[a] Hiroshi Miyashita,[a] Ryo Hanada,[a] Toshihiro Takashima[ab] and Haruna Kuroiwa[a]

[a.] *Integrated Graduate School of Medicine, Engineering, and Agricultural Sciences, University of Yamanashi, 4-3-11 Takeda, Kofu, Yamanashi 400-8511, Japan.*
[b.] *Clean Energy Research Center, University of Yamanashi, 4-3-11 Takeda, Kofu, Yamanashi 400-8511, Japan.*

Contents

ESI-1) Detailed preparation and characterization procedures.
ESI-2) XRD, UV-vis, SEM, STEM, and XPS characterization (Figs. S1, S2, S3, S4, and S5).
ESI-3) O_2 evolution resulting from half reaction of water catalyzed by $Ag_2V_4O_{11}$ (Table S1).
ESI-4) Complementary water-splitting test by $Ag_2V_4O_{11}$ (Fig. S6).
ESI-5) Summary of water-splitting activity of $Ag_2V_4O_{11}/ZnRh_2O_4$ (Table S2).
ESI-6) Stability of $Ag_2V_4O_{11}/ZnRh_2O_4$ with x = 0.7 before and after water-splitting reaction (Figs. S7, S8, and S9).
ESI-7) Solar-to-hydrogen energy conversion efficiency (STH, Fig. S10).
ESI-8) The energy band diagram of $Ag_2V_4O_{11}/ZnRh_2O_4$ and charge transfer process at 0 K (Fig. S11)
ESI-9) Additional comments for the advantages of the study over previously published papers.

ESI-1) Detailed preparation and characterization procedures.

A powdered photocatalyst composed of $Ag_2V_4O_{11}$ and $ZnRh_2O_4$ ($Ag_2V_4O_{11}/ZnRh_2O_4$) was prepared as follows. First, $Ag_2V_4O_{11}$ and $ZnRh_2O_4$ powders were synthesized using a solid-state reaction method. As starting materials, commercial Ag_2O (Kanto Kagaku; purity, 99.0%) and V_2O_5 (Kanto Kagaku; purity, 99.0%) powders were used for synthesizing $Ag_2V_4O_{11}$, and commercial ZnO (Wako; purity, 99.0%) and Rh_2O_3 (Kanto Kagaku; purity, 99.9%) powders were used for synthesizing $ZnRh_2O_4$. Stoichiometric amounts of the starting materials for both photocatalysts were wet-ball-milled for 20 h in polyethylene bottles using zirconium dioxide (ZrO_2) balls for milling. The resulting mixtures were calcined at 450 °C for 5 h and 1100 °C for 24 h to obtain $Ag_2V_4O_{11}$ and $ZnRh_2O_4$ powders, respectively, which were then thoroughly ground.

$Ag_2V_4O_{11}/ZnRh_2O_4$ powder was prepared as follows. $Ag_2V_4O_{11}$ and $ZnRh_2O_4$ (at molar ratios of 0.5, 0.7, 1.0 : 1.7) were wet-ball-milled as described above. The mixed powders were pressed at 60-kN force to form pellets, which were then heated at 450°C for 5 h. The pellets were ground into fine powder.

The crystal structures of the prepared powders were determined by X-ray diffraction (XRD) using a PW-1700 instrument (PANalytical). Ultraviolet photoelectron spectroscopy (UPS; Axis-Ultra, Shimadzu) was applied to determine the work function (WF) of $Ag_2V_4O_{11}$. Mott-Schottky analysis of $Ag_2V_4O_{11}$ was performed using a potentiostat (HZ-5000, Hokuto Denko Corp.) equipped with a frequency response analyzer. A platinum wire and a silver/silver potassium chloride electrode (Ag/AgCl/KCl sat.) were used as the counter and reference electrodes, respectively. The electrolyte was 0.5 M Na_2SO_4 aqueous solution (pH 6.8) and was purged with argon prior to each experiment. The working $Ag_2V_4O_{11}$ electrode was prepared by a squeegee method on fluorine-doped tin oxide (FTO) substrates. Then, the electrodes were annealed at 450 °C for 2 h. UV-visible absorption (UV-vis) spectra were obtained by the diffuse reflection method using a spectrometer (V-650, Jasco) and the one (UV-2600, Shimadzu) ranging from 300 to 800 nm and from 300 to 1400 nm, respectively, with barium sulfate ($BaSO_4$) as the reflectance standard. A scanning electron microscopy (SEM, JSM-6500F, JEOL Ltd.) system and scanning transmission electron microscopy (STEM, HD-2300, Hitachi High-Tech Corporation) were used to observe the morphology of the prepared photocatalysts. X-ray photoelectron spectroscopy (XPS; Axis-Ultra, Shimadzu) was applied to measure the Ag 3d, V 2p, Zn 2p, and Rh 3d core levels, constituent elements of $Ag_2V_4O_{11}/ZnRh_2O_4$. The obtained peaks were calibrated using the C 1s peak originated from a hydrocarbon surface contaminant that has a binding energy of 284.5 eV.

Tests of the photocatalytic O_2 evolution resulting from the half reaction of water and tests of photocatalytic overall water splitting were conducted in a gas-closed circulation system. Light-emitting diode (LED) lights with wavelengths of 700, 780, 850, 910, and 970 nm (hereafter, 700-, 780-, 850-, 910-, and 970-nm LEDs) were used. The 780-nm LED was LEDH60-780 (Hamamatsu Photonics), and the 700-, 850-, 910-, and 970-nm LEDs were bullet 700, 850, 910, and 970 nm of SPL-25-CC series (REVOX, Inc.), respectively; they were employed to irradiate monochromic lights. The amounts of H_2 and O_2 evolved were monitored using an online gas chromatograph (GC-8A, Shimadzu).

Regarding the photocatalytic O_2 evolution tests, $Ag_2V_4O_{11}$ powder (60 mg) with cerium sulfide ($Ce(SO_4)_2$, Kanto Kagaku, 0.1 mol/L) as a sacrificial agent was suspended in 12 mL of water without adjusting the pH of the solution and stirred using a magnetic stirrer. The 700-, 780-, 850-, and

910-nm LEDs were employed to confirm the evolution of O_2. The apparent quantum efficiency (AQE) for each wavelength was then evaluated. The AQEs for O_2 evolution were calculated using the equation AQE (%) = 100 × 4 × O_2 evolution rate/incident photon rate because the O_2 evolution is represented by the formula $2H_2O + 4h^+ \rightarrow O_2 + 4H^+$.

Regarding the photocatalytic overall water-splitting tests, $Ag_2V_4O_{11}/ZnRh_2O_4$ composite powder (60 mg) was suspended in 12 mL of pure water (pH unadjusted) in argon atmosphere (50 kPa) with constant stirring using a magnetic stirrer. The 700-, 780-, 850-, and 910-, and 970-nm LEDs were used for irradiation. The AQEs were calculated using the amount of O_2 evolved and the equation AQE (%) = 100 × 8 × O_2 generation rate/incident photon rate because O_2 generation in the two-step system is an eight-hole process. The AQEs were also calculated using the amount of H_2 evolved and the equation AQE (%) = 100 × 4 × H_2 generation rate/incident photon rate because H_2 generation in this system is a four-electron process (see Y. Sasaki, H. Nemoto, K. Saito and A. Kudo, *J. Phys. Chem. C*, 2009, **113**, 17536–17542). In addition, the overall water-splitting test was also performed by $Ag_2V_4O_{11}/ZnRh_2O_4$ with x of 0.7 under simulated sunlight irradiation (solar simulator (AM1.5), Asahi Spectra, HAL-320). Solar-to-hydrogen energy conversion efficiency (STH) was given by the equation STH (%) = $100 \times (R(H_2) \times \Delta G_r)/(P \times S)$ where $R(H_2)$, ΔG_r, P, and S denote the H_2 generation rate, the Gibbs energy of the water-splitting reaction (237 kJ mol^{-1}), the energy intensity of the AM1.5 solar irradiation (0.1 W cm^{-2}), and the irradiated sample area (7.5 cm^2), see Q. Wang, T. Hisatomi, Q. Jia, H. Tokudome, M. Zhong, C. Wang, Z. Pan, T. Takata, M. Nakabayashi, N. Shibata, Y. Li, I. D. Sharp, A. Kudo, T. Yamada and K. Domen, Nature Mater., 2016, **15**, 611–617.

ESI-2) XRD, UV-vis, SEM, STEM, and XPS characterization (Figs. S1, S2, S3, S4, and S5).

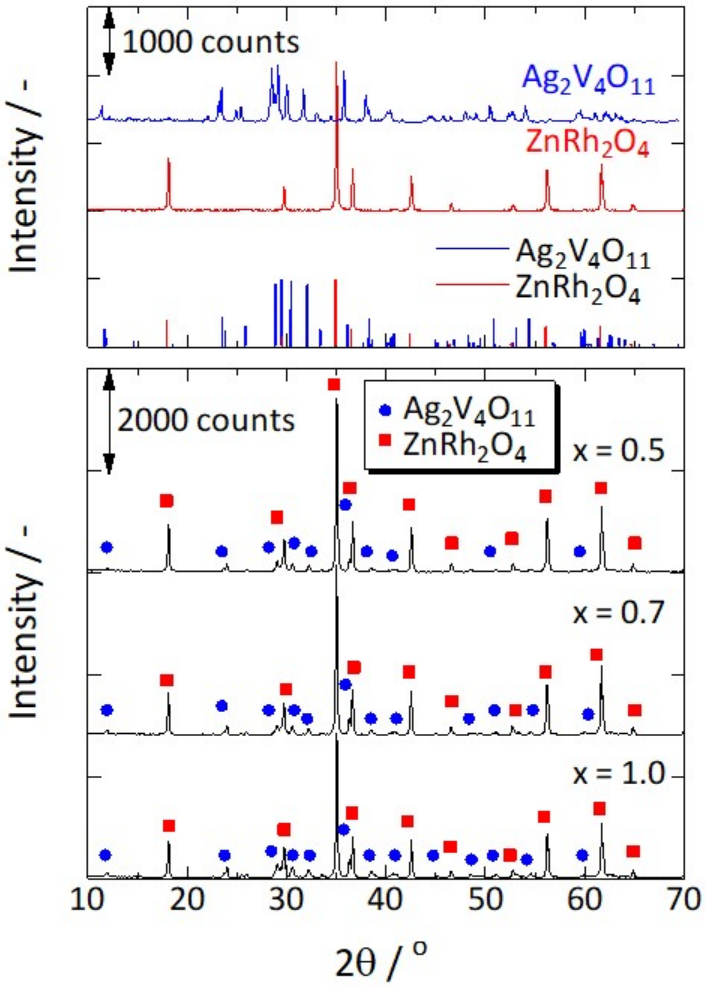

Fig. S1 XRD patterns of $Ag_2V_4O_{11}$, $ZnRh_2O_4$, and $Ag_2V_4O_{11}/ZnRh_2O_4$ with x values of 0.5, 0.7, and 1.0 prepared at a molar ratio of x : 1.7 ($Ag_2V_4O_{11}$: $ZnRh_2O_4$). The theoretical pattern of $Ag_2V_4O_{11}$ (blue vertical lines) is from the space group *C*2/*m* (monoclinic, No. 12) with lattice constants of *a* = 15.2936 Å, *b* = 3.5820 Å, *c* = 9.5370 Å, and beta = 127.862°, and that of $ZnRh_2O_4$ (red vertical lines) is from the space group F$d\bar{3}m$ (cubic, No. 227) with a lattice constant of *a* = 8.506 Å.

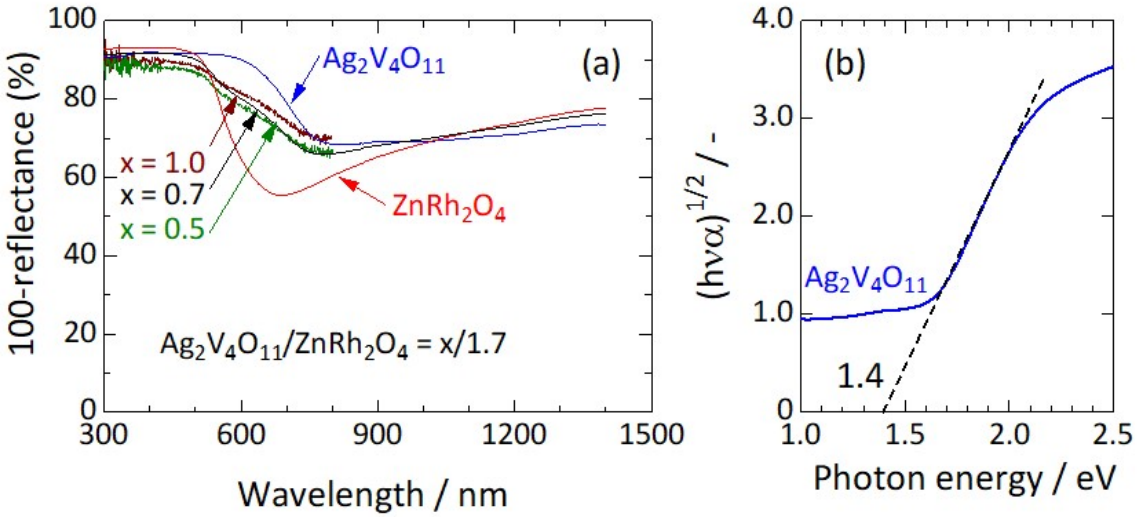

Fig. S2 (a) UV-vis spectra of $Ag_2V_4O_{11}$, $ZnRh_2O_4$, and $Ag_2V_4O_{11}/ZnRh_2O_4$ with x values of 0.5, 0.7, and 1.0 prepared at a molar ratio of x : 1.7 ($Ag_2V_4O_{11}$: $ZnRh_2O_4$). $Ag_2V_4O_{11}$, $ZnRh_2O_4$, and $Ag_2V_4O_{11}/ZnRh_2O_4$ with the x value of 0.7 were measured from 300 to 1400nm. $Ag_2V_4O_{11}/ZnRh_2O_4$ with x values of 0.5 and1.0 were measured from 300 to 800nm. (b) $(h\nu\alpha)^{1/2}$ plot for $Ag_2V_4O_{11}$ to obtain the bandgap energy to be 1.4 eV. The absorption coefficient α was estimated by the Kubelka-Munk conversion of reflectance.

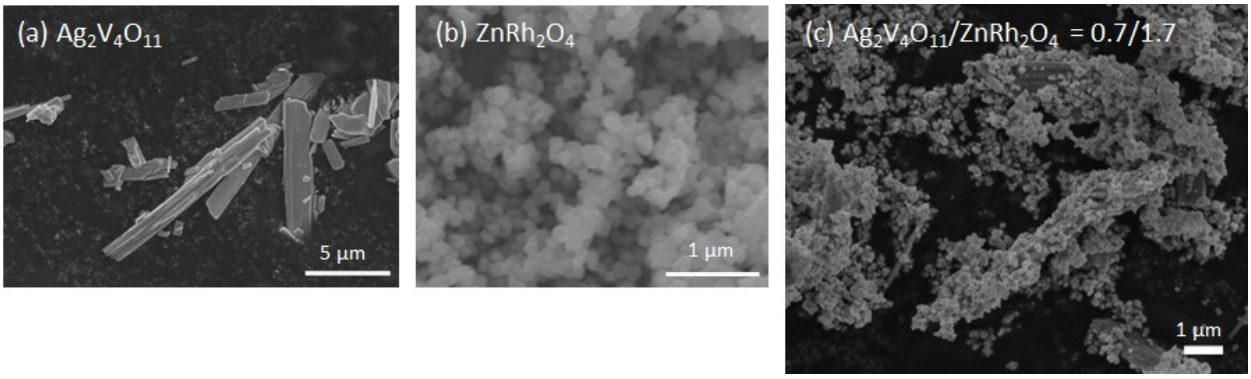

Fig. S3 SEM images of (a) $Ag_2V_4O_{11}$, (b) $ZnRh_2O_4$, and (c) $Ag_2V_4O_{11}/ZnRh_2O_4$ with x of 0.7.

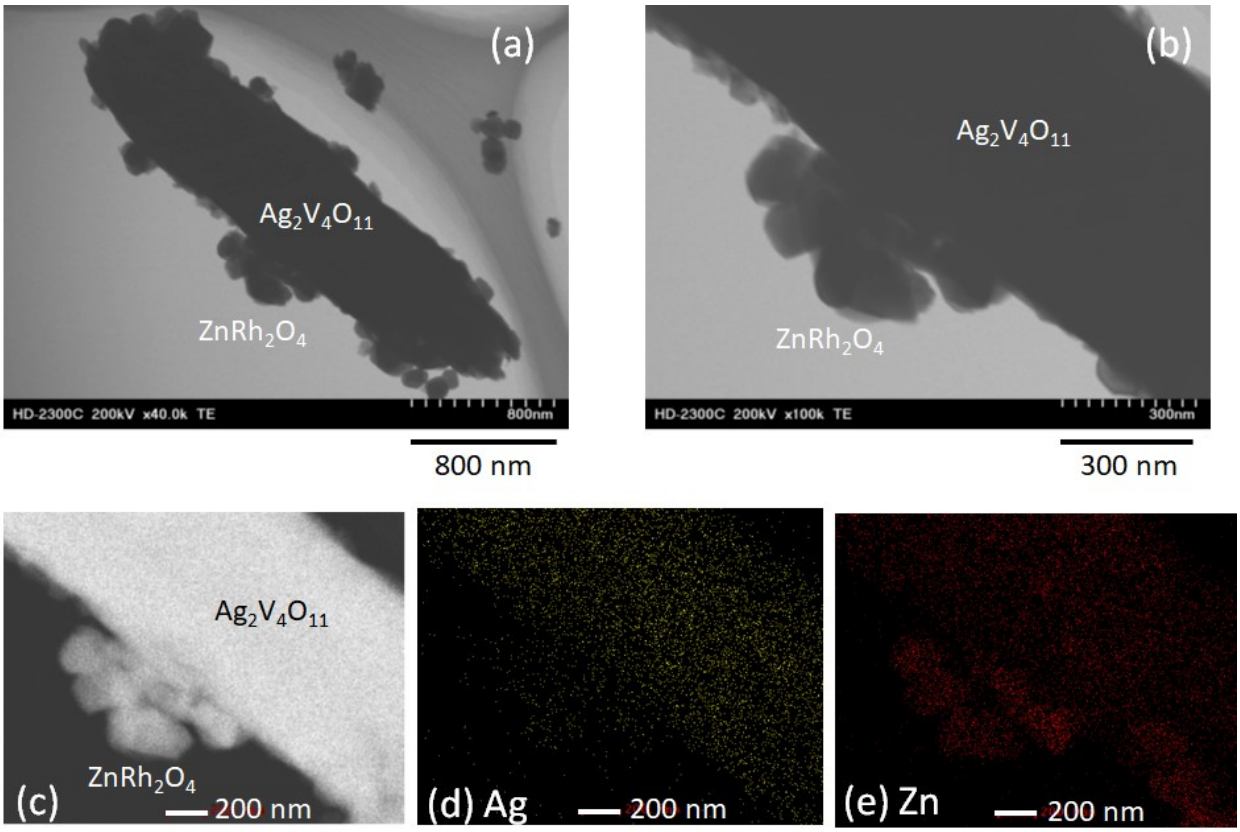

Fig. S4 STEM images of (a) $Ag_2V_4O_{11}/ZnRh_2O_4$ with x of 0.7 and (b) is the enlargement of (a). (d) and (e) EDS elemental maps, in which (d) yellow and (e) red colors correspond to Ag and Zn, respectively in the area of (c).

In Fig. S5a, Ad 3d spectra of Ag_2O and Ag are also included. Ag in $Ag_2V_4O_{11}$ was confirmed to be Ag^+. We have already reported that the spectra of V $2p_{3/2}$, Zn 2p, and Rh 3d in Ag-inserted heterojunction of bismuth vanadate ($Bi_4V_2O_{11}$) and $ZnRh_2O_4$ ($Bi_4V_2O_{11}$/Ag/$ZnRh_2O_4$).[7] The valency of V, Zn, and Rh were confirmed to be 5+, 2+, and 3+, respectively. The spectra of V $2p_{3/2}$, Zn 2p, and Rh 3d in $Ag_2V_4O_{11}$/$ZnRh_2O_4$ were identical to those in $Bi_4V_2O_{11}$/Ag/$ZnRh_2O_4$. So, V in $Ag_2V_4O_{11}$ was confirmed to be V^{5+}, and Zn and Rh were to be Zn^{2+} and Rh^{3+}, respectively. It should be noted that the peaks of the Ag $3d_{5/2}$ and Ag$3d_{3/2}$ spectra of $Ag_2V_4O_{11}$/$ZnRh_2O_4$ were 367.4 and 373.4 eV, respectively, and those of the Ag $3d_{5/2}$ and Ag$3d_{3/2}$ spectra of $Bi_4V_2O_{11}$/Ag/$ZnRh_2O_4$ were 368.7 and 374.7 eV, respectively. These differences are reasonable because Ag in $Bi_4V_2O_{11}$/Ag/$ZnRh_2O_4$ exists as Ag^0.

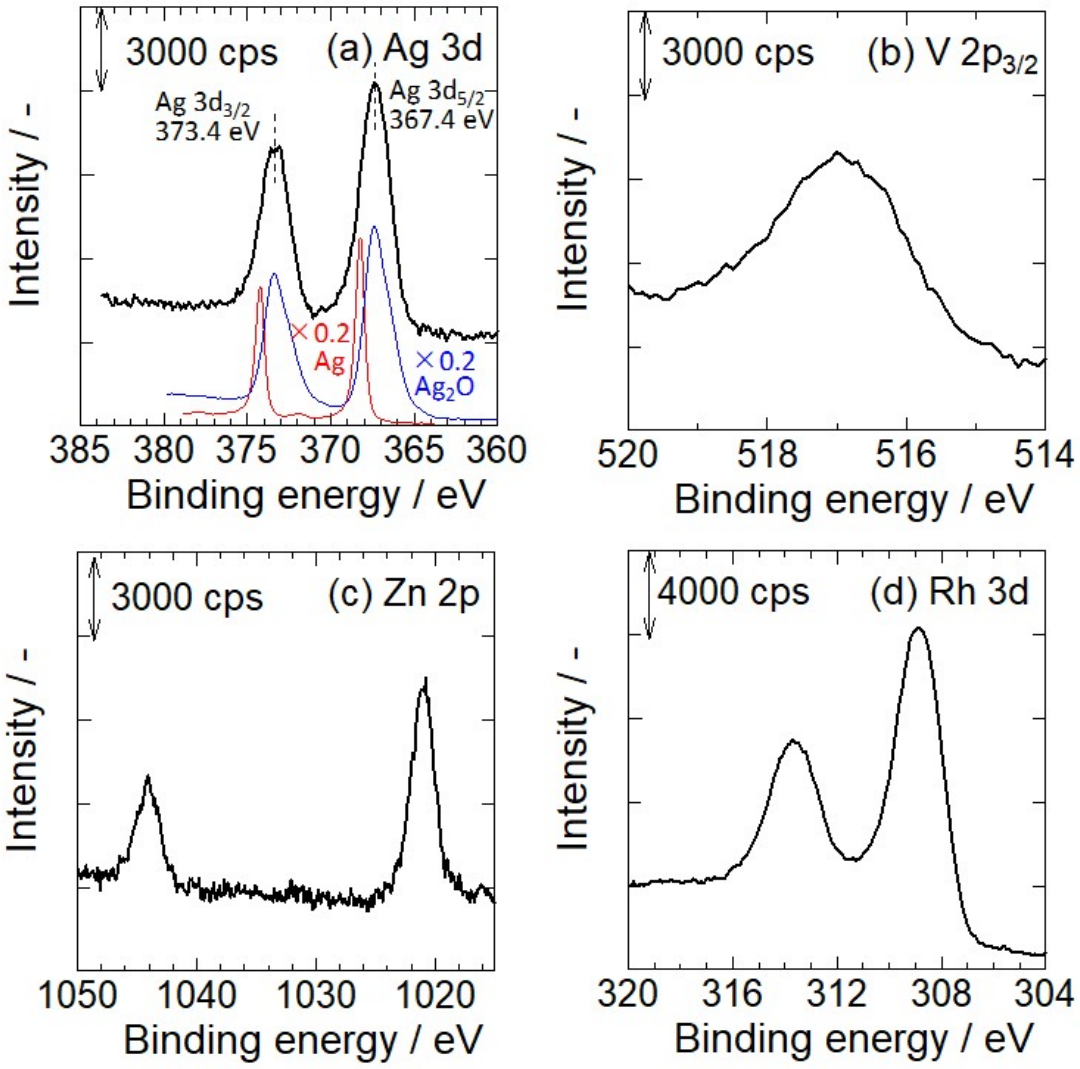

Fig. S5 XPS spectra of $Ag_2V_4O_{11}$/$ZnRh_2O_4$ with x of 0.7 for (a) Ag 3d, (b) V 2p, (c) Zn 2p, and (d) Rh 3d. In (a), Ad 3d spectra of Ag2O (blue) and Ag (red) are also included.

ESI-3) O_2 evolution resulting from half reaction of water catalyzed by $Ag_2V_4O_{11}$ (Table S1).

Table S1 Wavelengths, light intensities, incident photon rates, O_2 generation rates, and AQEs obtained from incident photon rates and O_2 generation rates of half-reaction of water.

Wavelength / nm	Light intensity / mW cm^{-2}	Incident photon rate / μmol h^{-1}	O_2 generation rate / μmol h^{-1}	Corrected O_2 generation rate / μmol h^{-1}	AQE (%)
700	2.2	3.4×10^{2}	1.3×10^{-2}	8.7×10^{-3}	1.0×10^{-2}
780	1.8	3.2×10^{2}	8.5×10^{-3}	4.7×10^{-3}	6.0×10^{-3}
850	8.0	1.5×10^{3}	6.5×10^{-3}	2.8×10^{-3}	7.2×10^{-4}
910	3.8	7.7×10^{2}	4.6×10^{-3}	7.7×10^{-4}	4.0×10^{-4}

Corrected O_2 generation rate is O_2 generation rate minus O_2 rate in the dark, 3.8×10^{-3} μmol h^{-1}.

ESI-4) Complementary water-splitting test by $Ag_2V_4O_{11}$ (Fig. S6).

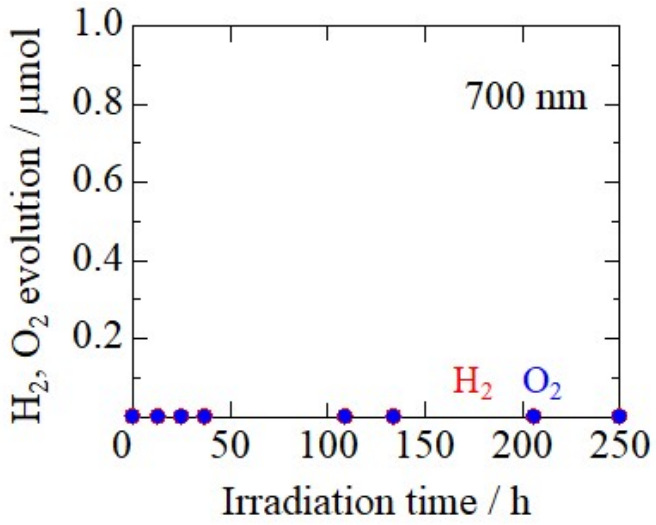

Fig. S6 Time courses of H_2 (red circles) and O_2 (blue circles) evolution from pure water in the presence of $Ag_2V_4O_{11}$ under irradiation with the 700-nm LED light. Neither H_2 nor O_2 was detected.

ESI-5) Summary of water-splitting activity of $Ag_2V_4O_{11}/ZnRh_2O_4$ (Table S2).

Table S2 AQEs of $Ag_2V_4O_{11}/ZnRh_2O_4$ (x= 0.5, 0.7, and 1.0 in x $Ag_2V_4O_{11}$–1.7 $ZnRh_2O_4$) under various monochromic light irradiation conditions with H_2 and O_2 generation rates.

Irradiated Light wavelength / nm	x	Light intensity / mW cm^{-2}	Incident photon rate /μmol h^{-1}	H_2 generation rate / μmol h^{-1}	AQE from H_2 (%)	O_2 generation rate / μmol h^{-1}	AQE from O_2 (%)
700	0.5	3.1	5.0×10^2	4.6×10^{-3}	3.7×10^{-3}	2.6×10^{-3}	4.1×10^{-3}
	0.7			6.7×10^{-3}	5.4×10^{-3}	3.7×10^{-3}	5.9×10^{-3}
	1.0			4.4×10^{-3}	3.5×10^{-3}	3.0×10^{-3}	4.8×10^{-3}
780	0.7	2.9	5.0×10^2	5.2×10^{-3}	4.2×10^{-3}	2.2×10^{-3}	3.5×10^{-3}
850	0.7	8.6	1.6×10^3	6.3×10^{-3}	1.5×10^{-3}	3.0×10^{-3}	1.5×10^{-3}
910	0.7	5.8	1.1×10^3	3.7×10^{-3}	1.3×10^{-4}	1.7×10^{-3}	1.2×10^{-3}

ESI-6) Stability of $Ag_2V_4O_{11}/ZnRh_2O_4$ with x = 0.7 before and after water-splitting reaction (Figs. S7, S8, and S9).

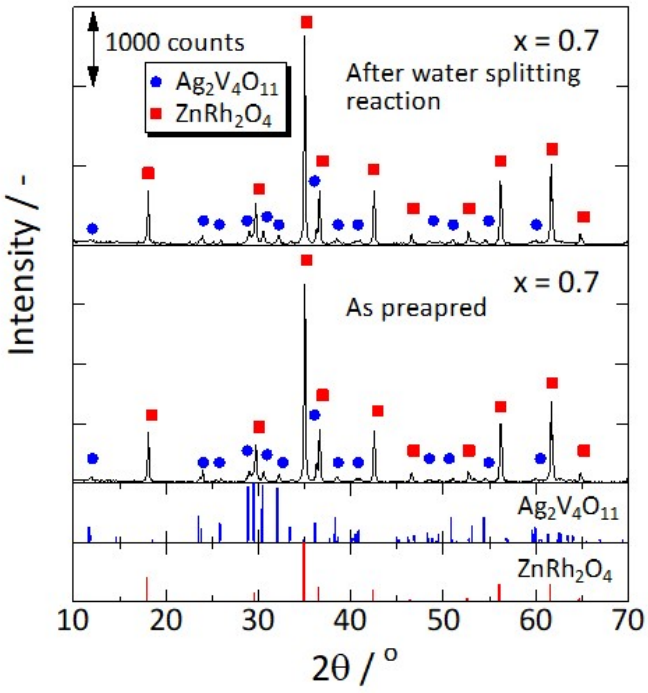

Fig. S7 XRD patterns of $Ag_2V_4O_{11}/ZnRh_2O_4$ with x of 0.7 before (as-prepared) and after the water-splitting reaction for 125 h irradiated with the 700-nm LED light. The XRD pattern of $Ag_2V_4O_{11}/ZnRh_2O_4$ with x of 0.7 before (as-prepared) the water-splitting reaction and the theoretical patterns of $Ag_2V_4O_{11}$ (blue vertical lines) and $ZnRh_2O_4$ (red vertical lines) are the same as those in Fig. S1.

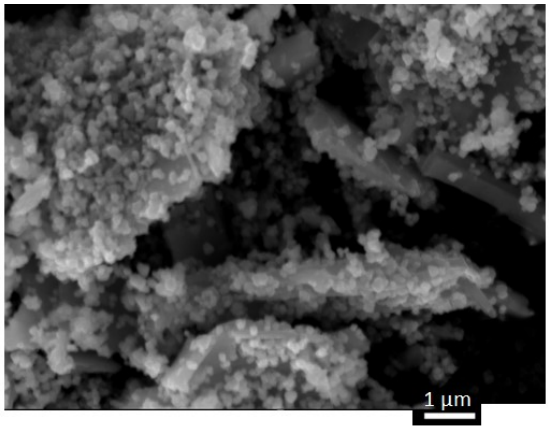

Fig. S8 SEM images of $Ag_2V_4O_{11}/ZnRh_2O_4$ with x of 0.7 after the water-splitting reaction for 125 h irradiated with the 700-nm LED light.

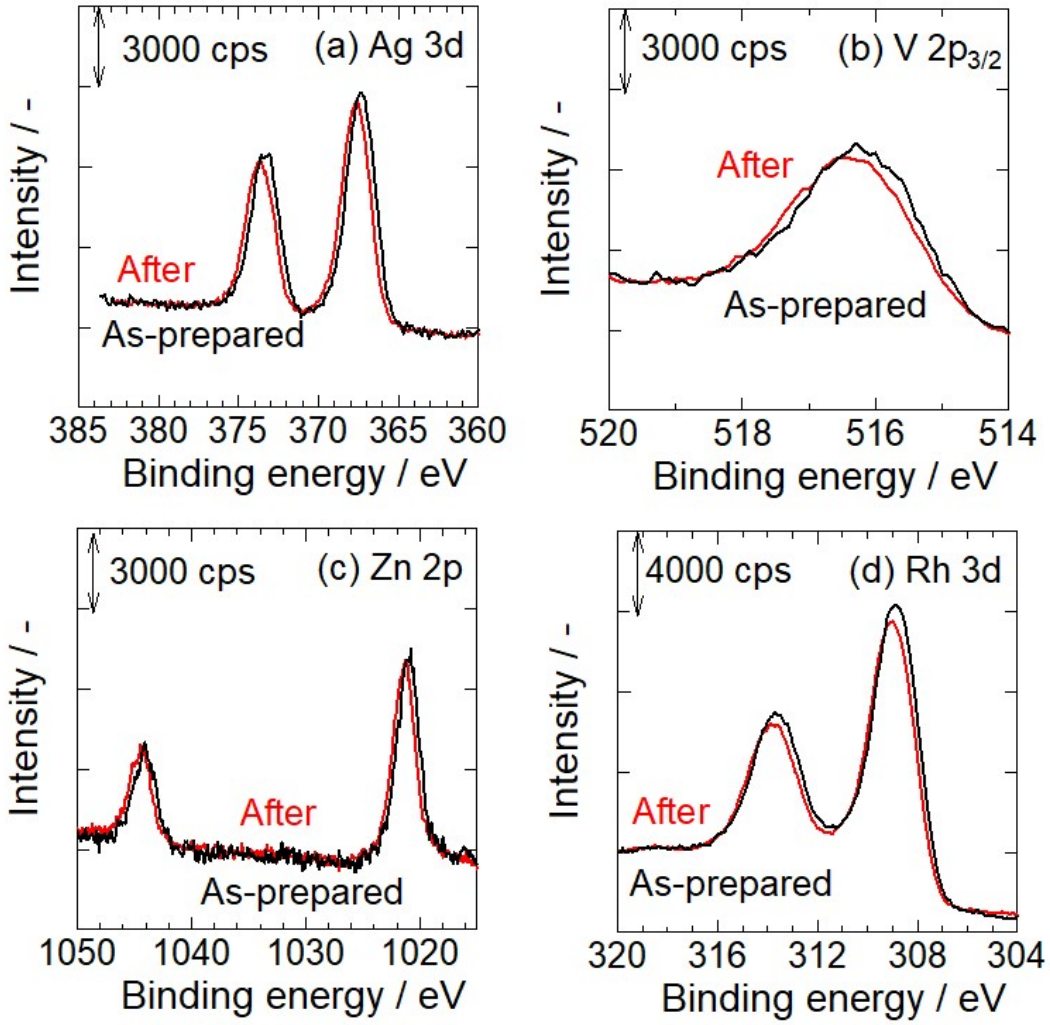

Fig. S9 Normalized XPS spectra of $Ag_2V_4O_{11}/ZnRh_2O_4$ with x of 0.7 for (a) Ag 3d, (b) V 2p, (c) Zn 2p, and (d) Rh 3d before (as-prepared, black) and after (red) the water-splitting reaction for 125 h irradiated with the 700-nm LED light. The XPS spectra before (as-prepared) the water-splitting reaction are the same as those in Fig. S5.

ESI-7) Solar-to-hydrogen energy conversion efficiency (STH, Fig. S10)

We examined the time courses of H_2 and O_2 evolution from distilled-water splitting by $Ag_2V_4O_{11}/ZnRh_2O_4$ with x = 0.7 under irradiation with a solar simulator as shown in Fig. S10. The amounts of H_2 and O_2 evolution having a ratio of 2 : 1 were observed from water, thereby accomplishing overall water splitting. The H_2 generation rate, $R(H_2)$, was 4.2×10^{-6} μmol s^{-1}, then solar-to-hydrogen energy conversion efficiency (STH) was 1.3×10^{-4}%.

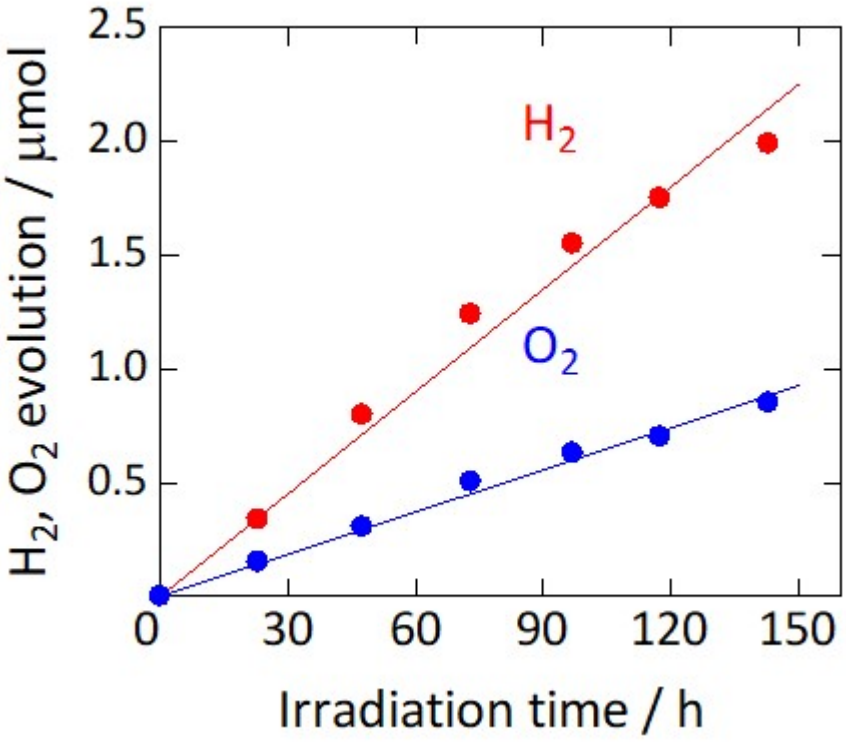

Fig. S10 Time courses of H_2 (red circles) and O_2 (blue circles) evolution from pure water by $Ag_2V_4O_{11}/ZnRh_2O_4$ with x of 0.7 under simulated sunlight irradiation (AM1.5).

ESI-8) The energy band diagram of $Ag_2V_4O_{11}/ZnRh_2O_4$ and charge transfer process at 0 K (Fig. S11)

A Fermi level (FL) changes depending on the temperature. At 0 K, the FL exists in the middle of the CB bottom potential of $Ag_2V_4O_{11}$ and its WF, and that in the middle of the VB top potential of $ZnRh_2O_4$ and its WF. After connecting $Ag_2V_4O_{11}$ and $ZnRh_2O_4$ at 0 K, FLs of each material also becomes the same, and accordingly, the CB bottom of $Ag_2V_4O_{11}$ and the VB top of $ZnRh_2O_4$ bend as shown in Fig. S4. With increasing the temperature, in the impurity-ion range, the FL of $Ag_2V_4O_{11}$ shifts positively, but does not exceed its WF (more negative than its WF) and that of $ZnRh_2O_4$ shifts negatively but does not exceed its WF (more positive than its WF). With further increasing the temperature, in the exhaustion range, the FL of $Ag_2V_4O_{11}$ shifts at more positive potential than its WF, and that of $ZnRh_2O_4$ shifts at more negative potential than its WF (Fig. 6). With further increasing the temperature, finally in the intrinsic range, the FLs of $Ag_2V_4O_{11}$ and $ZnRh_2O_4$ come to exist in the middle of each forbidden band.

After the connection of $Ag_2V_4O_{11}$ and $ZnRh_2O_4$, the band bending takes place because the "pinning" occurs at the interface between $Ag_2V_4O_{11}$ and $ZnRh_2O_4$, as indicated by green arrows in Fig. S4. So, the potential at this point is unchanged after the connection.

In every case, that is, at 0 K, in the impurity-ion range, in the exhaustion range, and in the intrinsic range, the band bending and the pinning take place although the degree of band bending changes.

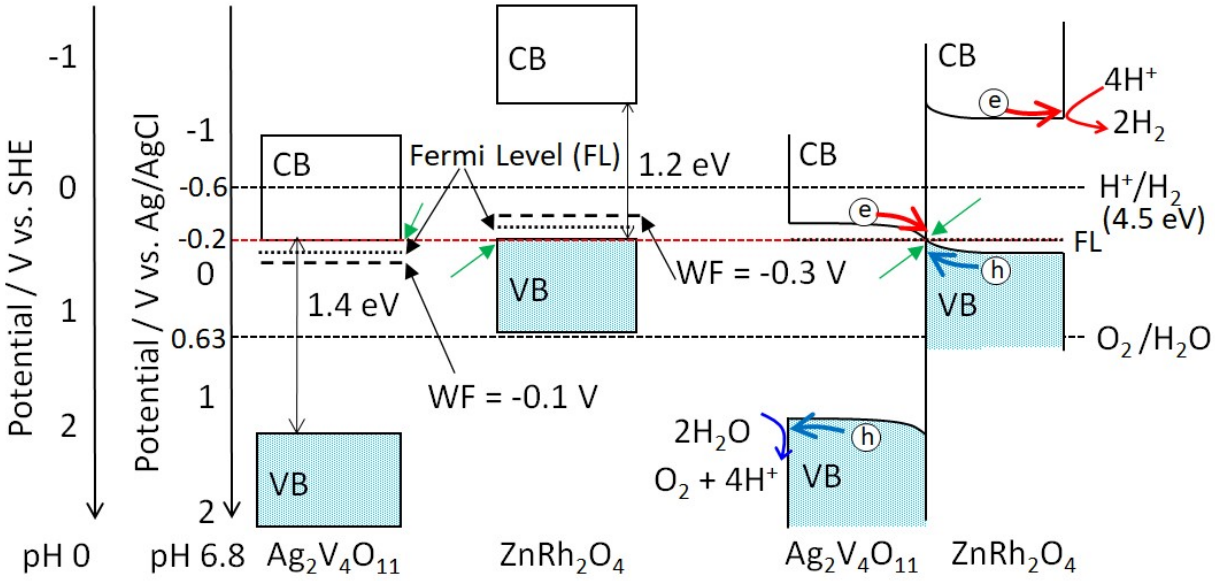

Fig. S11 Band edge positions of $Ag_2V_4O_{11}$ and $ZnRh_2O_4$ (left), and their band alignments after the connection of $Ag_2V_4O_{11}$ and $ZnRh_2O_4$ (right) at 0 K. The charge transfer processes are also shown. The WF of 4.5 eV corresponds to -0.6 V (*vs.* Ag/AgCl, pH 6.8).

ESI-9) Additional comments for the advantages of the study over previously published papers.

First, we compare the advantages of the work with OUR previously published papers. $Ag_2V_4O_{11}/ZnRh_2O_4$ in the present study has the advantages over our previously reported $ZnRh_2O_4/Ag/Bi_4V_2O_{11}$[6 (JMC A)] due to following three reasons; 1) AQE of $Ag_2V_4O_{11}/ZnRh_2O_4$ at 700 nm, 5.4–5.9×10^{-3}%, is higher than that of $ZnRh_2O_4/Ag/Bi_4V_2O_{11}$, 4.2–4.3×$10^{-3}$%, 2) $Ag_2V_4O_{11}/ZnRh_2O_4$ is sensitive to longer wavelength of up to 910 nm, and 3) $Ag_2V_4O_{11}/ZnRh_2O_4$ can be more facilely prepared in that the metallic Ag is not required to insert between $Ag_2V_4O_{11}$ and $ZnRh_2O_4$. Note that both $Ag_2V_4O_{11}/ZnRh_2O_4$ and $ZnRh_2O_4/Ag/Bi_4V_2O_{11}$ can split "pure" water (i.e., distilled water with no added chemicals).

Next, we compare the advantages of the work with previously published papers from groups except for ours. One of the approaches to visible-light sensitization of photocatalysts for overall water splitting is to construct a system composed of double photocatalysts sensitive to visible light, called the "Z-scheme", which was first reported by Sayama and coworkers, who used platinum (Pt)-deposited chromium-and-tantalum-codoped strontium titanate ($Pt/SrTiO_3$:Cr,Ta) as a H_2 evolution photocatalyst (H_2 photocatalyst) and Pt-deposited tungsten trioxide (Pt/WO_3) as an O_2 evolution photocatalyst (O_2 photocatalyst).[i] After that, numerous Z-scheme systems were reported in which various H_2 and O_2 photocatalysts were combined.[ii,iii] Most of these systems must employ a suitable redox mediator such as iodate ions (IO_3^-)/iodide ions (I^-) or ferric ions (Fe^{3+})/ferrous ions (Fe^{2+}). However, all the previously reported Z-scheme systems are only able to utilize visible light up to a wavelength of 520 nm. In addition, such conventional Z-scheme systems require a redox mediator, meaning that they are not capable of splitting pure water but capable of splitting water containing chemicals.

Recently, solid-state Z-scheme systems (ruthenium (Ru)-deposited rhodium-doped $SrTiO_3$ ($Ru/SrTiO_3$:Rh) and $BiVO_4$ [$Ru/SrTiO_3$:Rh-$BiVO_4$][iv], and $Ru/SrTiO_3$:Rh and photoreduced graphene oxide (PRGO)-loaded $BiVO_4$ ($PRGO/BiVO_4$) [$Ru/SrTiO_3$:Rh-$PRGO/BiVO_4$][v]) that functioned in the absence of a redox mediator were reported. In this case, PRGO acted as a as a solid-state electron mediator. However, they were still able to utilize visible light up to a wavelength of 520 nm. In addition, it was necessary to adjust the pH to 3.5 using sulfuric acid (H_2SO_4) to form contact between $Ru/SrTiO_3$:Rh and $BiVO_4$ and between $Ru/SrTiO_3$:Rh and $PRGO/BiVO_4$, so in this sense, pure-water splitting was not accomplished.

After that, directly connected composites of $Ru/SrTiO_3$:Rh and $BiVO_4$ [$Ru/SrTiO_3$:Rh-$BiVO_4$] was demonstrated to show photocatalytic activity for Z-schematic splitting of pure water (pH=7) under visible light without an electron mediator.[vi] However, the composites were able to utilize visible light up to a wavelength of 520 nm. Similar solid-state Z-scheme photocatalysts were reported one after another, *e.g.*, gold (Au)-inserted titanium dioxide (TiO_2) and $SrTiO_3$:Rh,[vii] carbon dots (CDs)-inserted cadmium sulfide (CdS) and $BiVO_4$,[viii] CDs-inserted nickel oxide (NiO) and $BiVO_4$,[ix] and molybdenum sulfide (MoS_2)-inserted CdS and zinc indium sulfide ($ZnIn_2S_4$),[x] where Au, CDs, and MoS_2 acted as a solid-state electron mediator. In addition, directly connected composites were reported, *e.g.*, graphitic carbon nitride (g-C_3N_4) and α-iron oxide (α-Fe_2O_3),[xi] $ZnIn_2S_4$ and tungsten oxide (WO_3).[xii,xiii] However, none of these can be sensitive to wavelength above 520 nm.

Thus, the $Ag_2V_4O_{11}/ZnRh_2O_4$ photocatalyst present has the advantage of being sensitive to 910-nm light, infrared light. However, at present the water-splitting activity of $Ag_2V_4O_{11}/ZnRh_2O_4$ is low. In this study, neither a cocatalyst for H_2 evolution nor that for O_2 evolution was utilized for $Ag_2V_4O_{11}/ZnRh_2O_4$. We have already reported that the selective loading of a H_2-evolution cocatalyst (Ag, Pt, Cu) onto $ZnRh_2O_4$ in $Bi_4V_2O_{11}/Ag/ZnRh_2O_4$ enhanced the water-splitting activity.[7,8] This method of enhancing the activity can be applied to $Ag_2V_4O_{11}/ZnRh_2O_4$. Such studies are currently underway in our laboratory.

References

i K. Sayama, K. Mukasa, R. Abe, Y. Abe and H. Arakawa, *J. Photochem. Photobiol. A: Chem.*, 2002, **148**, 71–77.

ii H. Kato, Y. Sasaki, A. Iwase and A. Kudo, *Bull. Chem. Soc. Jpn.*, 2007, **80**, 2457–2464.

iii A. Kudo, *Int. J. Hydrogen Energy*, 2002, **32**, 2673–2678.

iv Y. Sasaki, H. Nemoto, K. Saito, A. Kudo, *J. Phys. Chem. C*, 2009, **113**, 17536–17542.

v A. Iwase, Y. H. Ng, Y. Ishiguro, A. Kudo and R. Amal, *J. Am. Chem. Soc*., 2011, **133**, 11054–11057.

vi Q. Jia, A. Iwase and A. Kudo, *Chem. Sci.*, 2014, **5**, 1513–1519.

vii S. Wang, Y. Gao, Y. Qi, A. Li, F. Fan and C. Li, *J. Catal.*, 2017, **354**, 250–257.

viii X. Wu, J. Zhao, L. Wang, M. Han, M. Zhang, H. Wang, H. Huang, Y. Liu and Z. Kang, *Appl. Catal. B: Environ.*, 2017, **206**, 501–509.

ix C. Liu, Y. Fu, J. Zhao, H. Wang, H. Huang, Y. Liu, Y. Dou, M. Shao and Z. Kang, *Chem. Eng. J.*, 2019, **358**, 134–142.

x W. Chen, R.-Q. Yan, J.-Q. Zhu, G.-B. Huang and Z. Chen, *Appl. Surf. Sci.*, 2020, **504**, 144406.

xi X. She, J. Wu, J. Zhong, Y. Wang, Y. Song, K. Nie, Y. Liu, Y. Yang, M.-T. F. Rodrigues, R. Vajtai, J. Lou, D. Du, H. Li and P. M. Ajayan, *Adv. Energy Mater.*, 2017, **7**, 1700025.

xii Z. Li, J. Hou, B. Zhang, S. Cao, Y. Wu, Z. Gao, X. Nie and L. Sun, *Nano Energy*, 2019, **59**, 537–544.

xiii Y. Ding, D. Wei, R. He, R. Yuan, T. Xie and Z. Li, *Appl. Catal. B: Environ.*, 2019, **258**, 117948.